HHS Public Access

Author manuscript

*Acta Biomater*. Author manuscript; available in PMC 2023 August 11.

Published in final edited form as:

*Acta Biomater*. 2023 May ; 162: 240–253. doi:10.1016/j.actbio.2023.03.022.

# Multiscale characterization of left ventricle active behavior in the mouse

**Sunder Neelakantan**[a], **Mohit Kumar**[b], **Emilio A. Mendiola**[a], **Haley Phelan**[a], **Vahid Serpooshan**[c,d,e], **Sakthivel Sadayappan**[b], **Reza Avazmohammadi**[a,f,g,*]

[a] Department of Biomedical Engineering, Texas A&M University, College Station, TX, USA

[b] Department of Internal Medicine, Division of Cardiovascular Health and Disease, University of Cincinnati College of Medicine, Cincinnati, OH 45267, USA

[c] Department of Biomedical Engineering, Emory University School of Medicine and Georgia Institute of Technology, Atlanta, GA 30322, USA

[d] Department of Pediatrics, Emory University School of Medicine, Atlanta, GA 30322, USA

[e] Children's Healthcare of Atlanta, Atlanta, GA 30322, USA

[f] J. Mike Walker '66 Department of Mechanical Engineering, Texas A&M University, College Station, TX, USA

[g] Department of Cardiovascular Sciences, Houston Methodist Academic Institute, Houston, TX, USA

## Abstract

The myocardium possesses an intricately designed microarchitecture to produce an optimal cardiac contraction. The contractile behavior of the heart is generated at the sarcomere level and travels across several length scales to manifest as the systolic function at the organ level. While passive myocardial behavior has been studied extensively, the translation of active tension produced at the fiber level to the organ-level function is not well understood. Alterations in cardiac systolic function are often key sequelae in structural heart diseases, such as myocardial infarction and systolic heart failure; thus, characterization of the contractile behavior of the heart across multiple length scales is essential to improve our understanding of mechanisms collectively leading to depressed systolic function. In this study, we present a methodology to characterize the active behavior of left ventricle free wall (LVFW) myocardial tissues in mice. Combined with active tests in papillary muscle fibers and conventional in vivo contractility measurement at the organ level in an animal-specific manner, we establish a multiscale active characterization of the heart from fiber to organ. In addition, we quantified myocardial architecture from histology to shed light on the directionality of the contractility at the tissue level. The LVFW tissue activation-

* Corresponding author. sadayasl@ucmail.uc.edu (S. Sadayappan), rezaavaz@tamu.edu (R. Avazmohammadi).

Declaration of Competing Interest

Dr. Sadayappan provides consulting and collaborative research studies to the Leducq Foundation (CURE-PLAN), Red Saree Inc., Greater Cincinnati Tamil Sangam, Novo Nordisk, Pfizer, AavantiBio, AstraZeneca, MyoKardia, Merck and Amgen, but such work is unrelated to the content of this article. The remaining authors do not declare any conflicts of interest.

Supplementary material

Supplementary material associated with this article can be found, in the online version, at doi:10.1016/j.actbio.2023.03.022.

relaxation behavior under isometric conditions was qualitatively similar to that of the papillary muscle fiber bundle. However, the maximum stress developed in the LVFW tissue was an order of magnitude lower than that developed by a fiber bundle, and the time taken for active forces to plateau was 2–3 orders of magnitude longer. Although the LVFW tissue exhibited a slightly stiffer passive response in the circumferential direction, the tissues produced significantly larger active stresses in the longitudinal direction during active testing. Also, contrary to passive viscoelastic stress relaxation, active stresses relaxed faster in the direction with larger peak stresses. The multiscale experimental pipeline presented in this work is expected to provide crucial insight into the contractile adaptation mechanisms of the heart with impaired systolic function.

## 1. Introduction

The myocardium is a tissue with complex architecture enabling efficient pumping functionality in the heart. The passive and active behavior of the heart ventricles is primarily driven by the mechanical characteristics of the myocardium that, in turn, is determined by the behavior and microstructure of its internal components, including myofibers and collagen fibers. Ex-vivo characterization of myocardial tissues has been an important tool in improving the understanding of cardiac biomechanics in health and disease. Biaxial mechanical testing remains the standard for mechanical characterization of myocardial tissue, especially in small animals [1–3]. While the passive behavior of the myocardium has been extensively investigated, multiscale active contraction of the myocardium remains poorly studied. Myocardial contractility is generated at the sarcomere level, but is regulated by tissue content and architecture at larger length scales. Myocardial active and passive behaviors are also, by no means, independent, and the passive behavior influences active behavior through several mechanisms, including the dependency of active force generation and calcium sensitivity on passive stretching [4]. Structural heart diseases, such as myocardial infarction (MI) [5,6] and systolic heart failure (HF) [7,8], have been shown to initiate alterations in contractile patterns, affecting overall cardiac function. Thus, it is critical to develop an understanding of the mechanisms governing the contractile behavior of the myocardium in health and disease. Such investigation requires understanding the multiscale nature of contractile forces generated in the myocardium. The translation of contractile forces, developed in the myofibers, to the tissue level depends on the architecture of the myofibers integrated with the other extracellular components. At the tissue level, contractile forces combined with the geometry of the heart and the vascular resistance determine the contractile capacity of the organ. Advancing knowledge of how the contractile behaviors at different length scales of the myocardium are linked and effectively translate to the contractile capacity of the organ will allow for the identification of mechanistic biomarkers and improve the diagnostic, prognostic, and therapeutic tools in structural heart diseases.

The active contractile behavior of cardiac tissues has been studied previously in large animal models [9–12]. The majority of such studies have focused on using papillary muscles to represent the contractile behavior of the heart [9–11], and few studies have investigated the contractile behavior using myocardial tissue from the left ventricle (LV) [10,13]. Although papillary muscles lend themselves very well to one-dimensional active characterizations due

to their unidirectional anatomy and nearly aligned fibers, multiscale active characterization of the myocardium remains critically needed to identify underlying mechanisms by which the contractile behavior is impaired in a variety of structural heart diseases. In addition, although several constitutive laws have been developed to characterize the tissue-level active behavior in the myocardium [14,15], rigorous estimation of the involved material parameters depends on tissue-level active test data that is lacking in the literature.

In this study, we present a multiscale characterization of the contractile behavior of the murine heart at the fiber, tissue, and organ levels (Fig. 1). We further present the passive viscoelastic behavior of the heart at the tissue level and investigate the effect of *biaxial* passive stretch on contractile behavior. Our objective is to provide benchmark assays to characterize cardiac contractility at multiple length scales, from fiber to organ (Fig. 1), that can be used in studying a variety of structural heart diseases to identify and assess the multiscale mechanisms of contractility impairments. With this study, we intend to highlight the importance of the multiscale characterization of contractility in the heart to understand how contractility at different scales are related to each other. Findings from our study improve our understanding of the multiscale determinants of contractility in the LV and serve as an essential step in identifying high-fidelity multiscale performance metrics of LV contractility. Such measures will enhance the traditional measures of LV function that often lead to gross and limited information on cardiac performance. Ultimately, the development and implementation of our methods in disease models will allow for improved prognosis and the identification of new therapeutic targets in structural heart diseases.

## 2. Methods

### 2.1. Animal model

A total of 14 (male = 7, female = 7) 12- to 14-week-old C57BL/6 wild-type mice were used in this study. A cohort of 8 animals (4 male, 4 female) was used exclusively for in-vivo pressure-volume characterization of the LV through catheterization. The remaining 6 mice (3 male, 3 female) were used for ex-vivo experiments including biaxial testing followed by histological studies. As discussed in Section 2.2, to avoid any artifacts in tissue mechanical testing due to potential myocardial damage from invasive catheterization, we used a different cohort of mice (male = 3, female = 3) for the tissue and fiber testing that did not undergo catheterization. All experiments were conducted under guidelines approved by the University of Cincinnati Institutional Animal Care and Use Committee.

### 2.2. Organ-level contractility

In-vivo (organ-level) LV function was evaluated using a Transonic ADV500 pressure-volume (P-V) system and catheter (FTH-1212B-4018, Transonic Systems, Ithaca, NY). The mice were anesthetized with ketamine (50 g/g body wt i.p.) and inactin (100 g/g body wt i.p.), placed on a thermally controlled surgical table and ventilated via tracheostomy (200 L tidal volume, 160 breaths/min). The P-V catheter was introduced retrogradely into the LV via the right carotid and advanced to the LV apex. The calibration and parallel conductance offset of the volume signal was performed according to the manufacturers instructions. The pressure signal was calibrated after each experiment using a pressurized cuvette and mercury

manometer. All measurements were made while briefly turning off the ventilator to stabilize pressure and volume traces. After obtaining initial P-V measurements, end-systolic (ES) and end-diastolic (ED) P-V relationships were determined by briefly occluding the inferior vena cava (IVC) and producing alterations in venous return (preload) while measuring P-V loops. The end-systolic pressure-volume relationship (ESPVR) and end-diastolic pressure-volume relationships (EDPVR) were determined as the lines connecting the ES and ED points, respectively, from the P-V loops produced through IVC occlusion. End-systolic elastance (Ees), a measure of organ-level contractility, was calculated as the slope of the ESPVR. The hearts from animals used to measure organ-level contractility as described in this section were not utilized for tissue- and fiber-level contractility characterization. A separate cohort of animals was used to avoid artifacts from potential myocardial damage caused by invasive catheterization.

### 2.3. Relaxation and activation buffer

Myocardial relaxation and activation buffers and skinning methods were adopted from McNamara et al. [16]. Relaxation buffer was prepared by mixing 55.74 mM potassium propionate, 7 mM ethylene glycol bis (2-aminoethyl) tetraacetic acid, 100 mM N,N-bis(2-hydroxyethyl)-2-amino ethanesulfonic acid, 0.02 mM calcium chloride, 5.5 mM magnesium chloride, 5 mM dithiothreitol, 15 mM creatine phosphate, and 4.7 mM adenosine triphosphate. The pH was adjusted to 7.0 with 4 M potassium hydroxide and ionic strength was maintained at 180 with potassium propionate with pCa 9.0. The activation solution for the LVFW was prepared in the same way as the relaxation buffer, but with the addition of 7 mM calcium chloride to ensure pCa value of 4.5. Activation buffers with a range of pCa from 9 (relaxation buffer) to 4.5 (activation solution) were developed for papillary muscle tests. The range of pCa values was achieved through dilution of the activation solution with the relaxation buffer. Results from McNamara et al. [16] indicate the solutions described here are effective in activating and relaxing the myocardial tissue.

### 2.4. Tissue-level contractility

Following sacrifice, the heart was excised and the left ventricle free wall (LVFW) and papillary muscles were isolated. Full-thickness myocardium LVFW specimens (in the shape of rectangular slabs) were isolated from the mouse hearts ($n = 6$) with the slab edges being aligned with the longitudinal, circumferential, and radial directions of the LV (Fig. 2 A, B). Isolated LVFW specimens were first tested to characterize the passive myocardial properties, including biaxial tensile tests and biaxial stress relaxation tests, followed by active tests, as described below.

**2.4.1. Passive testing of LVFW—**The LVFW slab specimens were mounted in a biaxial mechanical testing machine (Cellscale Biotester, CellScale, Waterloo, Ontario, Canada) along circumferential and longitudinal directions, respectively (Fig. 2A). The myocardium specimens were submerged in the relaxation buffer at 22 °C during testing to prevent dehydration. Testing consisted of 10 cycles of preconditioning, followed by 10 cycles of testing in each of the three test protocols: (i) equibiaxial stretch, (ii) circumferential:longitudinal stretch ratio of 1:2, and (iii) circumferential:longitudinal stretch ratio of 2:1. The maximum stretch was set at 30% and the rate of loading set to 1% stretch

per second. The stress in this study was calculated as the ratio of force over an initial cross-sectional area represented by first Piola Kirchhoff stress (1st-PK). To calculate the tangent moduli, we initially fit the stress-stretch curve using a two-term exponential function $\left(P = f\left(\lambda\right) = a_1 e^{b_1 \lambda} + a_2 e^{b_2 \lambda} + c\right)$. The two-term exponential function was chosen because of its capacity to capture both low- and high-stretch behavior, especially slight inflections observed in the stress-stretch curves (Fig. 4). We estimated the goodness of the fits, and the $R^2$ was found to be greater than 99.0% in all the fits. The tangent modulus was calculated as the value of the derivative of this function $(\partial P / \partial \lambda)$. The low strain tangent modulus was calculated as the value of the derivative function at 5% stretch and the high strain tangent modulus was calculated at 30% stretch.

Characterization of the stress relaxation tests was performed after tensile testing. The passive viscoelasticity of the murine myocardium was characterized to compare and contrast to the active relaxation after measuring the tissue-level contractility. Force was measured as specimens were allowed to relax following loading to a maximum 30% stretch in three protocols: (i) equibiaxial stretch, (ii) circumferential:longitudinal stretch ratio of 1:2, and (iii) circumferential:longitudinal stretch ratio of 2:1. The relaxation modulus was computed as the slope of the stress-time curve at the start of the relaxation. In addition, the time to 90% relaxation was calculated as the time taken for the 1st PK stress to reach $P_{10}$ defined by

$$\frac{P_{10} - P_{\infty}}{P_{peak} - P_{\infty}} \leq 0.1 \tag{1}$$

Here, $P_{\infty}$ is the stress at the end of the relaxation phase where the stress has plateaued.

**2.4.2. Active testing of LVFW—**After characterization of the passive behavior of the myocardium, the specimens were chemically skinned by submerging them for 18 h at 4 °C in 10% Triton X-100 in relaxation buffer using a tilt shaker. After skinning, the specimens were gently cleansed by washing with fresh relaxation solution on ice for 10 min and were used for active testing within 12 h. The skinned specimens were mounted in the testing machine and held above the bath containing the activation solution. The specimens were sprayed with relaxation buffer to ensure specimens were fully relaxed. The specimens were then passively stretched (to 0, 10, and 20% stretch) at a rate of 1% stretch per second in air and held at this stretch until the force reading plateaued. The specimens were then slowly immersed into the activation solution at 22 °C and held for 10–15 min to allow the LVFW to fully contract and force to build up. Once the build-up force plateaued and the reading was stable for one minute, the specimens were slowly lifted out of the bath and sprayed with the relaxation buffer to record the relaxation behavior. The force reading approached zero and the specimens were shortened back to their original length by the end of the relaxation phase. This test was performed at different initial equibiaxial stretch values of 0%, 10%, and 20%, to determine the active force dependence on the tissue-level passive stretch.

The contraction and relaxation phases were separated manually from the raw active test data for further processing. First, the raw data was passed through a median filtering algorithm to reduce the noise. Next, given that the contraction and relaxation times were different for each specimen (due to varying LVFW thickness and extracellular content), those times

were normalized to be able to average the data. To normalize the data, the average time of contraction and relaxation was estimated. The average time of force build-up was 1055 ± 172 s and the average time of relaxation was 218.6 ± 101.5 s. Based on the mean values (1055 s and 218.6 for contraction and relaxation, respectively), the normalized time was split into 80% contraction and 20% relaxation. Each contraction and relaxation curve was then interpolated to a standard “normalized time” axis. The normalized curves are presented in the results section and for the sake of completeness, the original curves with 0% initial passive stretch have been presented in Fig. S1 in the supplementary materials. The relaxation modulus was calculated as the slope of the stress-time curve immediately at the start of the relaxation phase of the test. In addition, the relaxation time was calculated using Eq. (1).

## 2.5. Fiber-level contractility

The isolated papillary fibers from the same murine hearts ($n = 6$) were chemically skinned by submerging them for 12 h at 4 °C in 1% Triton X-100 in relaxation buffer using a tilt shaker. Specimens were then gently cleansed by washing with fresh relaxation solution on ice for 10 min and were used for testing within 12 h.

### 2.5.1. Active testing of papillary muscles—

Fiber-level contractility measurements were performed using the IonOptix calcium and contractility system (IonOptix, MA USA). Straight fiber bundles were isolated from the papillary muscles and attached at each end with aluminum t-clips (Fig. 2 E). Aluminum t-clips were used to attach the muscle fiber between a force transducer and length controller (Aurora Scientific Inc., Aurora, ON, Canada). Muscle dimensions (cross-sectional area and length) were determined using an ocular micrometer mounted in the dissection microscope (~ 10 μm resolution) and were used to normalize contractile force assuming an elliptical shape for the fiber cross-section. Sarcomere length was set to 2.1 μm with the assistance of the Aurora Scientific Video Sarcomere Length software. All force assays were performed in temperature-regulated baths set to 22 °C. Subsequently, the attached muscle fiber was exposed to a range of calcium solutions (pCa 9.0 to pCa 4.5) as determined by the Fabiato program [17]. The rate of force development after cross-bridge dissociation, denoted by $k_{tr}$, was assessed by allowing the papillary fiber to reach steady state force followed by imposing a 20% length shortening over 20 ms followed by a rapid (~1 ms) stretch back to its original length [16,18]. $k_{tr}$ was calculated by fitting the force redeveloped in the fiber after this slack-stretch treatment against the time required for a one-phase association curve.

## 2.6. Architectural characterization

After active testing, specimens ($n = 6$) were fixed in 10% formalin for 48 h and then stored in 70% ethanol. The specimens were sectioned transmurally with a slice thickness of 5 μm every 80 μm and stained with picrosirius red (PSR) stain, turning myofibers yellow and collagen fibers red. These specimens were mounted on slides and then imaged using Olympus VS120 Virtual Slide Scanning System to obtain images at 20x zoom. The images were used to calculate the distribution of myofiber angles as a function of transmural depth using methods described in our previous work [3,19]. Briefly, the Beta distribution functions of myofiber angles were calculated at each depth level and were stacked together to obtain the fiber distribution as a function of transmural depth [20].

### 2.7. Statistical analysis

The experimental data was analyzed in Microsoft Excel and GraphPad Prism 9. All the data are represented as mean ± standard error of mean. Both male and female mice were included in the study with filled and hollow markers indicating male and female specimens, respectively. Paired student t-tests were performed when analyzing the statistical significance between the circumferential and longitudinal directions in Figs. 4B, 5C–E, and 7B, D. The data presented in Fig. 7A, C was analyzed using two-way ANOVA with repeated measures using the mixed effect model with Tukey's correction when performing statistical analysis with a dependent variable. Significance was accepted at $p < 0.05$. For this study, we have chosen to report the numerical significance values [21].

## 3. Results

### 3.1. Hemodynamics

The results from echocardiography and left heart catheterization were used to establish baseline organ function and to interpret tissue-level contractile function. Results indicated a mean ejection fraction of 75.42 ± 5.17% and end-systolic pressure values of 87.41 ± 5.45 mmHg (Fig. 3, Table 1). From the ESPVR line was plotted for the representative occlusion curve and the end-systolic elastance ($E_{es}$) (slope of the ESPVR line) was found to be 2139 mmHg/ml (Fig. 3b).

### 3.2. Tissue-level passive behavior

Passive testing of the LVFW specimens prior to skinning indicated that the murine LVFW exhibits comparable stress behaviors along circumferential and longitudinal directions with mean circumferential stress of 16.35 kPa and mean longitudinal stress of 14.66 kPa at 30% equibiaxial stretch (Fig. 4A). Under equibiaxial stretch above 25% stretch, the specimens were slightly biased towards the circumferential direction, indicated by the calculated tangent modulus (Fig. 4B). However, no significant difference in the mean tangent modulus was apparent when comparing the circumferential and longitudinal directions. Non-equibiaxial stretch results also indicate tissue specimens exhibit similar behavior when stretched to the same extent (Fig. 4C), although the calculated tangent modulus indicates a slight bias in the longitudinal direction (Fig. 4D).

The stress relaxation tests also indicated myocardial specimens' passive viscoelastic behavior is similar in both the circumferential and longitudinal directions, as seen from the similarity of the stress relaxation curves (Fig. 5A–B). The representative results from stress relaxation tests with unequal initial stretch are presented in Fig. 5B. The difference between the circumferential and longitudinal directions under equibiaxial stretching decrease further when the specimen is allowed to passively relax (Fig. 5A). The reduction in the difference between the circumferential and longitudinal stresses was evident when the stresses at the beginning of the relaxation (peak) and once plateaued (terminal) were compared (Fig. 5C). Similar viscoelastic behavior is also indicated by the relaxation time (Fig. 5D) and short-term relaxation rate behavior (Fig. 5E).

### 3.3. Tissue-level contractility

Contractile tests indicated the LVFW specimens are actively contracting (Fig. 6) due to the presence of $Ca^{2+}$ and the stress build-up over time was qualitatively similar to the curves observed during testing of myofiber bundles [10,11]. The tissue specimens were present in the activation solution for 215 ± 95 s before a significant increase in contractile force was observed (Fig. S1). Also, the specimens were present in the activation solution for 1055 ± 72 s before the contractile stress fully plateaus and the relaxation phase begins. The contractile stress developed due to activation was larger in the longitudinal direction at all initial pre-stretches (Fig. 6A–C). The presented plots were normalized on the time axis to allow for averaging of the plots 6A) as described in Section 2.4.2. Without any prior passive stretch, the specimens developed mean peak stress values of 2.36 kPa and 4.58 kPa along the circumferential and longitudinal directions, respectively. Results also indicated the development of peak active stress is accelerated with increasing passive stretch values (Fig. 6D).

A significant increase in the peak total stress was observed when the initial passive stretch increased from 0% to 10% and then 20% (Fig. 7A). Peak total stress increased 3-fold and 2-fold in the circumferential and longitudinal directions, respectively, in the specimens with 20% initial stretch when compared to specimens with no initial stretch. The active portion of the total stress was calculated as active stress = plateaued stress-initial stress. The comparison of active stresses for different initial stretches revealed that the increase in active stress when the initial stretch changes from 10% to 20% was greater in comparison to the increase when the initial stretch changes from 0% and 10% (Fig. 7C). This indicates that the relationship between active stress and initial stretch is non-linear. The peak total stress values indicated that the difference between male and female specimens was only significant for 0% initial stretch in the circumferential direction (Fig. 7A). Considering only the active stress part, the difference between sexes is significant at 0 and 10% initial stretch in the circumferential direction (Fig. 7C).

The LVFW tissue relaxed faster in the longitudinal direction compared to the circumferential direction (Fig. 7B). The circumferential relaxation was more gradual than longitudinal relaxation, as seen by the smaller relaxation modulus (Fig. 7D), although the difference in relaxation modulus is not apparent in the representative plots due to the lower maximum stress in the circumferential direction. For the relaxation time and modulus (Figs. 5C, D), no significant difference was observed between male and female specimens.

### 3.4. Fiber-level contractility

The maximum stress generated by the papillary muscles was 42.3 ± 1.46 kPa (Fig. 8A). The maximum force remained constant beyond pCa = 5.0, indicating $Ca^{2+}$ (Fig. 8B) saturation in the papillary muscles. $k_{tr}$ values were found to be 7.95 ± 0.89 $s^{-1}$ (Fig. 8C) and time to achieve maximum contractile force was 1 sec (Fig. 8D).

### 3.5. Myofiber architecture

Histological slices were analyzed to produce regional and transmural myofiber orientation presented by heat maps across the LVFW. The mean fiber angles in each transmural layer

were found to be 30.97 ± 17.12° at the endocardium, 10.31 ± 15.7° at the midwall, and −19.38 ± 17.11° at the epicardium (Fig. 9F). The histological analysis indicated a consistent trend in all specimens exhibiting a shift in myofiber angle towards the longitudinal direction when moving transmurally from the epicardium to the endocardium. The myofiber helical range (the transmural rotation of myofiber orientation) among the six specimens was found to be 50.6 ± 16.5°.

## 4. Discussion

### 4.1. Multiscale characterization of contractile behavior

Organ-level contractile behavior, and its influence on cardiac function, are fundamentally dependent on the multiscale nature of myocardial contractile behavior. Individual myofiber contraction contributes to the contraction of the LVFW, leading to the contraction of the LV and the ejection of blood into the aorta. The contractile capability of the ventricle is affected by various details at all length scales, including myofiber architecture, extracellular matrix content, passive properties of the LVFW, and so on. Hence it is important to perform *subject-specific* contractility tests at multiple length scales to understand the mechanisms of contractile load transfer from the sarcomere level to the organ-level systolic function and how the mechanisms are impaired in disease. However, multiscale investigations of the contractile behavior of the LV, especially those including tissue-level contractile behavior, remain critically scarce in the literature. Such investigations appear to be even more limited in small animals as existing studies have primarily made use of large animal models. Although studies in large animals are important to investigate the behavior of the healthy heart, they may be limited in performing comprehensive studies of many structural heart diseases for which small animal models serve as an essential preclinical step. To the best of our knowledge, the study we have presented here is the first to investigate the contractile behavior of the LV at multiple length scales in small animals. We investigated the contractile behavior of murine LV, from fiber to organ, to understand the translation of force generated by the myofibers to the contraction in the LV. Our work serves as an important step toward a comprehensive understanding of active myocardial mechanics that can be supplemented by a multiscale model in the future to bridge the behavior observed at these length scales.

### 4.2. Contrast between passive and active myocardial anisotropy

Passive mechanical testing revealed comparable behavior of the LVFW in the circumferential and longitudinal direction with a modest bias towards the circumferential direction, consistent with the quantification of helical angle found to be biased towards the circumferential direction. The stress values observed were also consistent with our previous studies [22,23]. In contrast to the passive stress anisotropy, the active contraction tests resulted in significantly larger stress in the longitudinal direction that appears to be at odds with the myofibers orientation quantification. As described in the following, there are several mechanisms that could contribute to having a larger contractile stress in the longitudinal direction despite the bias of the fiber orientation toward the circumferential direction. First, multiple studies have found variations in contractility across the transmural depth in human and porcine myocardial tissue [24–27]. Given the transmural variation in myofiber orientation (Fig. 9), higher active forces in the endocardial and epicardial regions,

compared to the midwall regions, would contribute to larger active stress in the longitudinal direction. We plan to investigate the transmural variation of contractile stresses in the LVFW tissue in future studies. For this investigation, fresh LVFW tissue would be sectioned into multiple sections using a method adapted from lung tissue preparation [28]. We plan to use the precision cut lung slicing (PCLS) technique on the LVFW samples to isolate the endocardium, myocardial midwall, and epicardium. The sectioned specimens will be skinned separately and tested using the process described in Section 2.4.2.

Second, related to the above mechanism, possible incomplete skinning of the midwall could add to the contrast between active circumferential and longitudinal stresses. Since the middle layers were the most biased towards the circumferential direction, incomplete skinning of this region would reduce the contractile forces generated in the circumferential direction. Radial sectioning of the fresh LVFW specimen into two or three layers using PCLS (discussed above) and performing the active test on each section separately could clarify the potential contribution of incomplete skinning to the circumferential-longitudinal stress contrast as detailed more in Limitations. Third, our LVFW specimens were longer in the circumferential direction as compared to the longitudinal direction (4317 ± 395 μm vs 3854 ± 254 μm). This difference necessitates force to be translated over a larger distance in the circumferential direction. Myofibers contain intercalated discs which allow the fibers to branch and merge into one another. This network across the myocardial tissue is expected to reduce and diffuse the force compared to a nearly unidirectional fiber arrangement in papillary muscles with a lower level of fiber branching. Microstructural models (such as those presented in Li et al. [29]) can provide more insights into the difference between the force level generated in individual fibers and the tissue. And, lastly, fibers in the myocardial tissue have a transverse (out-of-plane) fiber orientation that could reduce the force measured in the biaxial plane [30–32]. We did not measure the transverse orientation for our specimens in this work as we performed sectioning and histology in the radial direction. However, the transverse orientation is estimated to be up to 20°for murine specimens [32]. The bias of the transverse orientation relative to the circumferential and longitudinal directions would further differentiate these two active stresses in the circumferential-longitudinal plane. Overall, further experimental studies are needed in the future to investigate the transmural variation of contractile forces and active versus passive stress anisotropy.

Testing the contractile behavior with an initial passive stretch revealed that the contractile force developed by the LVFW is dependent on its passive stretch (sarcomere length), consistent with prior studies on isolated muscle fiber specimens [33,34] and with the widely recognized Frank-Starling law. The net stress generated by the LVFW specimen significantly increased along both the circumferential and longitudinal directions at 20% initial stretch (Fig. 7A). We did not exceed an initial passive stretch of 20% to reduce the risk of damage to the tissue during active contraction, but we expect a turning point in the behavior of the developed active stress at larger initial stretches consistent with the length dependency observed in fiber-level experiments [34,35]. In addition, there were contrasts between passive viscoelastic relaxation and active relaxation behaviors. The passive relaxation rates and times were similar in the circumferential and longitudinal directions (Fig. 5E), whereas there was a significant difference in the active relaxation rate between the two directions

(Fig. 7C). The difference in the active relaxation times was reduced in the presence of an initial pre-stretch. This observation points to the dependence of active relaxation on the passive behavior of the myocardium which has significant implications in cardiac diseases with impaired relaxation. For instance, this dependence may imply that slow relaxation in diastolic heart failure may be in part due to changes in the passive behavior of the myocardium.

### 4.3. Fiber-level versus tissue-level active stress

Papillary muscle fiber-level testing indicated maximum contractile stress was an order of magnitude higher than the maximum stress at the tissue level along both longitudinal and circumferential directions. The reduction in active forces from fiber to tissue can be attributed in part to the presence of non-contractile constituents at the tissue level, including collagen fibers, vascular network, and amorphous ground extracellular matrix. Myocardial tissue contains 25% non-contractile components by volume [36,37] that can reduce the contractile stress by the same percentage according to the rule of mixture for connective tissues. Representative histological slices of the tissue from our study (Fig. S3) indicated the presence of up to 28.9% of extracellular matrix. Further reductions in tissue-level contractile stress can be explained due to the transmural variation of the fibers across the LVFW specimens and lack of cross-fiber active stress explained in the following through an idealized fiber composite example. Let us consider a composite block with 10 layers. Let the fiber orientation vary linearly from 70° to −70° (resembling a representative variation from the endocardium to the epicardium [32]). Following the assumptions of affine conditions and equal volume fraction for each layer, the tissue-level stress can be obtained as

$$\sigma_{Tissue} = \mathbf{Q}^{\mathbf{T}}(\theta)\sigma_{Layer}\mathbf{Q}(\theta) \text{ with } \mathbf{Q}(\theta) = \begin{bmatrix} \cos\theta & -\sin\theta \\ \sin\theta & \cos\theta \end{bmatrix}, \tag{2}$$

where the fiber-generated stress in each layer is given by

$$\sigma_{Layer} = \begin{bmatrix} \sigma_f & 0 \\ 0 & 0 \end{bmatrix}, \tag{3}$$

and $\theta$ is the average fiber orientation in each layer. By doing the calculations, one can arrive at 43% and 60% reductions in the tissue-level circumferential and longitudinal stresses, respectively, when compared to the fiber-level stress $\sigma_f$. Another important mechanism involved in the reduction of contractile stress is the transverse (out-of-plane) orientation of myofibers, described in Section 4.2. The study by Schmitt et al. [32] measured the fiber angles in murine hearts using diffusion tensor imaging and found the transverse angle in the LVFW to be in the range of 10–20°. Equations (2) and (3) can be used in this case to estimate the reduction of force caused by the presence of an out-of-plane myofibers orientation. Here, $\sigma_{Layer}$ is the total stress produced by the myofiber and $\theta$ is set to the out-of-plane angle. Following a similar transformation rule as in Eqs. (2) and (3) and setting $\theta = 15^{\circ}$, one arrives at an estimated 8% reduction in the force value measured in the circumferential-longitudinal plane. These cumulative reductions can explain the level of reductions from fiber stress to tissue-level stress observed in our data. Further reductions in the circumferential stress can be, at least in part, attributed to the mechanisms described

in Section 4.2, including branching and railway-like network of myofibers across the myocardium, and potential skinning of midwall layers.

### 4.4. Tissue-level versus organ-level active stress

The ex-vivo measurements of stress in contracting myocardial tissues can be contrasted with conventional organ-level approximations of total stress in a beating LV. One can estimate the in-vivo myocardial wall stress in the LV using the Laplace equation given by $\sigma = \mathrm{Pr}/2t$ where $\sigma$ is the Cauchy-like wall stress, $r$ is the LV approximate radius, and $t$ is the LV wall thickness. Using the mean healthy murine data $P = 80$ mmHg at end-systole, $= 4$ mm, and $t = 2$ mm, the circumferential wall stress is approximated as $\sigma = 10.6$ kPa (80mmHg). 6 kPa (80 mmHg). Noting that our tissue stresses were presented as the 1st-PK stress **P**, the Laplace stress estimate $\sigma$ can be converted to the 1st-PK stress **P** through

$$\mathbf{P} = J\sigma\mathbf{F}^{-\mathbf{T}} \tag{4}$$

where **F** is the deformation gradient tensor and $J = 1$ denotes the volumetric deformation. Approximate values for **F** can be obtained from the study by Hoffman et al. [38], where cardiac strains in mice were estimated through speckle tracking analysis of images from echocardiography. Using an isotropic representation of and $\sigma = \sigma\mathbf{I}$ where **I** is an identity matrix, we obtain circumferential and longitudinal stress values of around 12 kPa, which is in a similar range as that of ex-vivo contractile stress. We have also presented the multiscale translation of contractile stress in the supplementary information from the fiber to the organ level (Fig. S2). This observation highlights the applicability of multiscale ex-vivo studies of contractility in the LV myocardium to improve our understanding of LV contractility in health and disease.

In addition to our comparisons between tissue-level stress measurements and the organ-level stress estimations, it is worth noting several studies that have used electromechanical models to study the relationship between the fiber-level stress and organ-level function in the LV [27,39,40]. Such studies have commonly used fiber-level contractile stress to estimate organ-level function or vice versa using phenomenological constitutive models. For instance, the fiber-level contractile stresses used in the study by Land et al. [39] for the organ-level model were set at 42.6 kPa, which is comparable to the contractile stresses measured from our papillary muscle testing. In addition, we have estimated fiber-level stress of 30 kPa in our previous computational rodent studies using animal-specific hemodynamic data [19,41].

### 4.5. Comparisons between contraction and relaxation times

The time taken by the LVFW tissues to reach the peak stress was found to be about three orders of magnitude greater than that of the isolated papillary muscles. This difference can be viewed in light of the fact that the rate of activation is primarily driven by the rate of diffusion of $Ca^{2+}$. The rate of diffusion is significantly faster in the skinned papillary muscle as there is a higher surface-to-volume ratio. In addition, intracellular $Ca^{2+}$ is actively absorbed by the sarcoplasmic reticulum (SR), and this process requires ATP, which is present in both the activation and relaxation buffers. During activation (stress build-up), there is excess $Ca^{2+}$ in the solution, and the inward diffusion of $Ca^{2+}$ to the cell is entirely

driven by “passive” diffusion process till the $Ca^{2+}$ concentration reaches equilibrium. In contrast, when the LVFW specimen is removed from the bath and sprayed with the relaxation buffer, there is a significant and sharp decrease in the extracellular $Ca^{2+}$ due to “active” ATP-driven uptake of $Ca^{2+}$ into the SR that rapidly decreases the concentration of intracellular $Ca^{2+}$. We also expect this ATP-driven uptake of $Ca^{2+}$ to be one of the reasons for the significant delay in generating contractile forces at the tissue level. Papillary muscles reach maximum tension significantly faster due to both higher rates of diffusion (due to a higher surface-to-volume ratio), and lower uptake of $Ca^{2+}$ due to the less extensive SR network in the papillary muscle as compared to the LV myocardium [42].

### 4.6. Implications

Heart diseases such as systolic and diastolic heart failure cause significant alterations to the contractile-relaxation behavior of the myocardium, leading to impaired cardiac function. Characterization of the contractile behavior at the tissue level is essential to advance our understanding of how contractility translates from fiber to tissue, and then to the organ, and to identify the multiscale mechanisms impairing proper coordination of myofiber-extracellular matrix interaction leading to insufficient contractility at the organ level. Also, the development of proper protocols and apparatus to characterize tissue-level contractility proves crucial in the advancement of cardiac tissue engineering to generate contractile tissues mimicking native tissues used to study cardiac diseases or for therapeutic purposes such as cardiac patches [43–45]. The results we have presented here call for the investigation of transmural and regional variations in myocardial contractility. This is particularly important to develop treatments that may affect certain transmural regions of the LVFW, such as myocardial infarction. In addition to investigating LV contractility, this method can be used to study RV contractility in health and disease. Conditions such as pulmonary hypertension alter RV free wall (RVFW) contractility and often lead to right heart failure. We have used this method towards the initial investigation of heart failure in transgenic mice [46] and have observed similar trends as those observed in the papillary muscle tests [16]. Additionally, the contractility at the tissue level and its variability through the transmural thickness are important factors to be added to predictive models to improve their accuracy. Predictive models have used multiple approaches to model LV and RV functions [47–49] in health and disease, and incorporating information regarding contractility at multiple length scales into such models would significantly improve model accuracy and allow the rigorous prediction of changes in contractility that occur during functional adaptation of the heart.

### 4.7. Limitations

A different cohort of mice, but with a similar stain and age, was used for invasive catheterization to characterize organ-level contractility to avoid erroneous data due to potential myocardial damage caused by catheterization. We plan to verify the impact of catheterization in a future study with a larger cohort of mice. Although the skinning process for the LVFW specimens was performed over a period of 18 h, LVFW specimens may still not have been fully skinned.. Incomplete skinning could potentially lead to lower active force readings or heterogeneous contraction of the specimen due to the partial presence of membrane structures preventing diffusion of $Ca^{2+}$. We plan to verify the the success of our

skinning technique in our future studies where we investigate the transmural variation of contractile stresses developed in the LVFW. We propose two types of tests, (i) transmural sectioning using PCLS and techniques adapted from Liu et al. [28], and (ii) dividing LVFW specimens into two to three parts and testing each part with a specific concentration to find the proper concentration range at which the LVFW tissue show the max contraction indicating that the skinning has properly removed the membranes. Changes in “porosity” was investigated in limited histological sections of skinned and unskinned specimens to evaluate potential damage to the tissue due to skinning (reported in Fig. S4). Further investigation in a larger cohort of skinned and unskinned murine specimens is needed in the future to determine proper statistical differences in porosity. Studies have reported that the $Ca^{2+}$ sensitivity of cardiac tissue is dependent on the temperature [50,51]. Harrison and Bers [50] reported an 18% increase in maximum tension developed in the cardiac tissue of rabbits when the temperature is increased from 22 °C to 36 °C. Future studies will be tested at 36 °C to understand the temperature sensitivity at the tissue level. The number of animals used for tissue-level testing of contractile stress is limited, especially when isolated to a single sex. Further testing is required with a larger cohort of mice to better characterize the sex differences in the contractile behavior of the myocardium. The movement of the LVFW specimens into and out of the activation bath led to slight spikes in force readings during testing. These values were filtered out to isolate the timewise tissue behavior, and parameter calculations were performed, ignoring such measurement artifacts.

## 5. Conclusion

In this study, we presented a multiscale approach to characterize the contractility of murine LV. We presented detailed methodology and results to characterize *combined passive and active behavior* of murine LVFW specimens at the tissue level which appears to be overwhelmingly understudied. We integrated tissue-level tests with the study of the contractile behavior at the fiber level, and the study of organ-level contractility in a similar cohort of mice, to provide a complete multiscale assessment of the LV contractility from fiber to organ. We expect this study to serve as an assay to assess and improve our understanding of multiscale contractility impairments observed in a variety of structural heart diseases.

## Supplementary Material

Refer to Web version on PubMed Central for supplementary material.

## Acknowledgments

This work was supported by the National Institutes of Health (K99HL138288 and R00HL138288 to R.A. and R01 HL131017–05A1 to V.S. and R01 AR078001, R01 HL130356, R01 HL105826, R38 HL155775, and R01 HL143490 to S.S.). Dr. Sadayappan has received support from the American Heart Association 2019 Institutional Undergraduate Student (19UFEL34380251) and Transformation (19TPA34830084) awards, the PLN Foundation (PLN crazy idea) and the Leducq Foundation (Transatlantic Network 18CVD01, PLN-CURE). We would like to thank Dr. Maziyar Keshavarzian for his algorithm to plot myofiber distribution frequency. We would also like to acknowledge the assistance of the Integrated Microscopy and Imaging Laboratory at the Texas A&M College of Medicine.

## Data availability

The data that support the findings of this study are available from the corresponding author, R.A., upon request.

## References

[1]. Fomovsky G, Thomopoulos S, Holmes J, Contribution of extracellular matrix to the mechanical properties of the heart, J. Mol. Cell. Cardiol. 48 (3) (2010) 490–496. [PubMed: 19686759]

[2]. Hill MR, Simon MA, Valdez-Jasso D, Zhang W, Champion HC, Sacks MS, Structural and mechanical adaptations of right ventricle free wall myocardium to pressure overload, Ann. Biomed. Eng. 42 (12) (2014) 2451–2465. [PubMed: 25164124]

[3]. Neelakantan S, Xiang Q, Chavan S, Li K, Ling X, Dixon RA, Sacks M, Vanderslice P, Avazmohammadi R, Abstract 14303: structural remodeling in the left ventricular myocardium underlies systolic dysfunction in myocardial infarction, Circulation 144 (Suppl_1) (2021) A14303.

[4]. Golob M, Moss R, Chesler N, Cardiac tissue structure, properties, and performance: a materials science perspective, Ann. Biomed. Eng. 42 (10) (2014) 2003–2013. [PubMed: 25081385]

[5]. Zhang H, Chen X, Gao E, MacDonnell SM, Wang W, Kolpakov M, Nakayama H, Zhang X, Jaleel N, Harris DM, Li Y, Tang M, Berretta R, Leri A, Kajstura J, Sabri A, Koch WJ, Molkentin JD, Houser SR, Increasing cardiac contractility after myocardial infarction exacerbates cardiac injury and pump dysfunction, Circ. Res. 107 (6) (2010) 800–809. [PubMed: 20671241]

[6]. McComb C, Carrick D, McClure JD, Woodward R, Radjenovic A, Foster JE, Berry C, Assessment of the relationships between myocardial contractility and infarct tissue revealed by serial magnetic resonance imaging in patients with acute myocardial infarction, Int. J. Cardiovasc.Imaging 31 (6) (2015) 1201–1209. [PubMed: 26047771]

[7]. Lou Q, Fedorov VV, Glukhov AV, Moazami N, Fast VG, Efimov IR, Transmural heterogeneity and remodeling of ventricular excitation-contraction coupling in human heart failure, Circulation 123 (17) (2011) 1881–1890. [PubMed: 21502574]

[8]. Campbell SG, Haynes P, Kelsey Snapp W, Nava KE, Campbell KS, Altered ventricular torsion and transmural patterns of myocyte relaxation precede heart failure in aging F344 rats, Am. J. Physiol.-HeartCirc. Physiol. 305 (5) (2013) H676–H686.

[9]. Saeki Y, Sagawa K, Suga H, Transient tension responses of heart muscle in Ba2+ contracture to step length changes, Am. J. Physiol.-HeartCirc. Physiol. 238 (3) (1980) H340–H347.

[10]. Marban E, Kusuoka H, Yue DT, Weisfeldt ML, Wier WG, Maximal Ca2+-activated force elicited by tetanization of ferret papillary muscle and whole heart: mechanism and characteristics of steady contractile activation in intact myocardium, Circ. Res. 59 (3) (1986) 262–269. [PubMed: 2429779]

[11]. Shibata T, Berman MR, Hunter WC, Jacobus WE, Metabolic and functional consequences of barium-induced contracture in rabbit myocardium, Am. J. Physiol.-HeartCirc. Physiol. 259 (5) (1990) H1566–H1574.

[12]. Livingston JZ, Resar JR, Yin FC, Effect of tetanic myocardial contraction on coronary pressure-flow relationships, Am. J. Physiol.-HeartCirc. Physiol. 265 (4) (1993) H1215–H1226.

[13]. Lin DHS, Yin FCP, A multiaxial constitutive law for mammalian left ventricular myocardium in steady-state barium contracture or tetanus, J. Biomech. Eng. 120 (4) (1998) 504–517. [PubMed: 10412422]

[14]. Guccione JM, McCulloch AD, Mechanics of active contraction in cardiac muscle: Part I constitutive relations for fiber stress that describe deactivation, J. Biomech. Eng. 115 (1) (1993) 72–81. [PubMed: 8445901]

[15]. Guccione JM, Waldman LK, McCulloch AD, Mechanics of active contraction in cardiac muscle: Part II cylindrical models of the systolic left ventricle, J. Biomech. Eng. 115 (1) (1993) 82–90. [PubMed: 8445902]

[16]. McNamara JW, Singh RR, Sadayappan S, Cardiac myosin binding protein-c phosphorylation regulates the super-relaxed state of myosin, Proc. Natl. Acad. Sci. 116 (24) (2019) 11731–11736. [PubMed: 31142654]

[17]. Fabiato A, Computer programs for calculating total from specified free or free from specified total ionic concentrations in aqueous solutions containing multiple metals and ligands, in: Biomembranes Part Q: ATP-Driven Pumps and Related Transport: Calcium, Proton, and Potassium Pumps, in: Methods in Enzymology, Vol. 157, Academic Press, 1988, pp. 378–417. [PubMed: 3231093]

[18]. Colson BA, Locher MR, Bekyarova T, Patel JR, Fitzsimons DP, Irving TC, Moss RL, Differential roles of regulatory light chain and myosin binding protein-c phosphorylations in the modulation of cardiac force development, J. Physiol. 588 (6) (2010) 981–993. [PubMed: 20123786]

[19]. Mendiola EA, Neelakantan S, Xiang Q, Merchant S, Li K, Hsu EW, Dixon RAF, Vanderslice P, Avazmohammadi R, Contractile adaptation of the left ventricle post-myocardial infarction: predictions by rodent-specific computational modeling, Ann. Biomed. Eng. (2022).

[20]. Avazmohammadi R, Hill MR, Simon MA, Zhang W, Sacks MS, A novel constitutive model for passive right ventricular myocardium: evidence for myofiber–collagen fiber mechanical coupling, Biomech. Model. Mechanobiol. 16 (2) (2017) 561–581. [PubMed: 27696332]

[21]. Althouse AD, Below JE, Claggett BL, Cox NJ, de Lemos JA, Deo RC, Duval S, Hachamovitch R, Kaul S, Keith SW, Secemsky E, Teixeira-Pinto A, Roger VL, null null, Recommendations for statistical reporting in cardiovascular medicine: a special report from the american heart association, Circulation 144 (4) (2021) e70–e91. [PubMed: 34032474]

[22]. Keshavarzian M, Neelakantan S, McAlister L, Leatherman A, Frazier S, Tong CW, Avazmohammadi R, Abstract 14317: left ventricular free wall adaptations in heart failure with preserved ejection fraction: Insights from a murine model, Circulation 144 (Suppl_1) (2021) A14317.

[23]. Neelakantan S, Mendiola E, Burton A, Sadayappan S, Wang Z, Avazmohammadi R, Stress relaxation behavior of left ventricular myocardium in mice, FASEB J. 36 (S1) (2022).

[24]. van der Velden J, Klein L, van der Bijl M, Huybregts M, Stooker W, Witkop J, Eijsman L, Visser C, Visser F, Stienen G, Isometric tension development and its calcium sensitivity in skinned myocyte-sized preparations from different regions of the human heart, Cardiovasc. Res. 42 (3) (1999) 706–719. [PubMed: 10533611]

[25]. Stelzer JE, Norman HS, Chen PP, Patel JR, Moss RL, Transmural variation in myosin heavy chain isoform expression modulates the timing of myocardial force generation in porcine left ventricle, J. Physiol. 586 (21) (2008) 5203–5214. [PubMed: 18787035]

[26]. Haynes P, Nava KE, Lawson BA, Chung CS, Mitov MI, Campbell SG, Stromberg AJ, Sadayappan S, Bonnell MR, Hoopes CW, Campbell KS, Transmural heterogeneity of cellular level power output is reduced in human heart failure, J. Mol. Cell. Cardiol. 72 (2014) 1–8. [PubMed: 24560668]

[27]. Wang H, Zhang X, Dorsey SM, McGarvey JR, Campbell KS, Burdick JA, Gorman JH, Computational investigation of transmural differences in left ventricular contractility, J. Biomech. Eng. 138 (11) (2016) 1145011–1145016. [PubMed: 27591094]

[28]. Liu G, Betts C, Cunoosamy DM, Åberg PM, Hornberg JJ, Sivars KB, Cohen TS, Use of precision cut lung slices as a translational model for the study of lung biology, Respir. Res. 20 (1) (2019) 162. [PubMed: 31324219]

[29]. Li DS, Mendiola EA, Avazmohammadi R, Sachse FB, Sacks MS, A high-fidelity 3D micromechanical model of ventricular myocardium, in: Ennis DB, Perotti LE, Wang VY (Eds.), Functional Imaging and Modeling of the Heart, Springer International Publishing, Cham, 2021, pp. 168–177.

[30]. Scollan DF, Holmes A, Winslow R, Forder J, Histological validation of myocardial microstructure obtained from diffusion tensor magnetic resonance imaging, Am. J. Physiol.-HeartCirc. Physiol. 275 (6) (1998) H2308–H2318.

[31]. Geerts L, Bovendeerd P, Nicolay K, Arts T, Characterization of the normal cardiac myofiber field in goat measured with mr-diffusion tensor imaging, Am. J. Physiol.-HeartCirc. Physiol. 283 (1) (2002) H139–H145.

[32]. Schmitt B, Fedarava K, Falkenberg J, Rothaus K, Bodhey NK, Reischauer C, Kozerke S, Schnackenburg B, Westermann D, Lunkenheimer PP, Anderson RH, Berger F, Kuehne T, Three-dimensional alignment of the aggregated myocytes in the normal and hypertrophic murine heart, J. Appl. Physiol. 107 (3) (2009) 921–927. [PubMed: 19628727]

[33]. Allen DG, Jewll BR, Murray JW, The contribution of activation processes to the length–tension relation of cardiac muscle, Nature 248 (5449) (1974) 606–607. [PubMed: 4824032]

[34]. Julian FJ, Sollins MR, Sarcomere length-tension relations in living rat papillary muscle, Circ. Res. 37 (3) (1975) 299–308. [PubMed: 1157219]

[35]. ter Keurs HE, Iwazumi T, Pollack GH, The sarcomere length-tension relation in skeletal muscle, J. Gen. Physiol. 72 (4) (1978) 565–592. [PubMed: 309929]

[36]. Vliegen HW, Van Der Laarse A, Cornelisse CJ, Eulderink F, Myocardial changes in pressure overload-induced left ventricular hypertrophy: a study on tissue composition, polyploidization and multinucleation, Eur. Heart J. 12 (4) (1991) 488–494. [PubMed: 1829680]

[37]. Camelliti P, Borg TK, Kohl P, Structural and functional characterisation of cardiac fibroblasts, Cardiovasc. Res. 65 (1) (2005) 40–51. [PubMed: 15621032]

[38]. Hoffman M, Kyriazis ID, Lucchese AM, de Lucia C, Piedepalumbo M, Bauer M, Schulze PC, Bonios MJ, Koch WJ, Drosatos K, Myocardial strain and cardiac output are preferable measurements for cardiac dysfunction and can predict mortality in septic mice, J. Am. Heart Assoc. 8 (10) (2019) e012260. [PubMed: 31112430]

[39]. Land S, Niederer SA, Aronsen JM, Espe EKS, Zhang L, Louch WE, Sjaastad I, Sejersted OM, Smith NP, An analysis of deformation-dependent electromechanical coupling in the mouse heart, J. Physiol. 590 (18) (2012) 4553–4569. [PubMed: 22615436]

[40]. Zhang X, Liu Z-Q, Campbell KS, Wenk JF, Evaluation of a novel finite element model of active contraction in the heart, Front. Physiol. 9 (2018) 425. [PubMed: 29740338]

[41]. Avazmohammadi R, Mendiola EA, Soares JS, Li DS, Chen Z, Merchant S, Hsu EW, Vanderslice P, Dixon RAF, Sacks MS, A computational cardiac model for the adaptation to pulmonary arterial hypertension in the rat, Ann. Biomed. Eng. 47 (1) (2019) 138–153. [PubMed: 30264263]

[42]. Tesi C, Piroddi N, Colomo F, Poggesi C, Relaxation kinetics following sudden Ca2+ reduction in single myofibrils from skeletal muscle, Biophys. J. 83 (4) (2002) 2142–2151. [PubMed: 12324431]

[43]. Fujimoto KL, Tobita K, Merryman WD, Guan J, Momoi N, Stolz DB, Sacks MS, Keller BB, Wagner WR, An elastic, biodegradable cardiac patch induces contractile smooth muscle and improves cardiac remodeling and function in subacute myocardial infarction, J. Am. Coll. Cardiol. 49 (23) (2007) 2292–2300. [PubMed: 17560295]

[44]. Serpooshan V, Zhao M, Metzler SA, Wei K, Shah PB, Wang A, Mahmoudi M, Malkovskiy AV, Rajadas J, Butte MJ, Bernstein D, Ruiz-Lozano P, The effect of bioengineered acellular collagen patch on cardiac remodeling and ventricular function post myocardial infarction, Biomaterials 34 (36) (2013) 9048–9055. [PubMed: 23992980]

[45]. Jiang Y, Sun S-J, Zhen Z, Wei R, Zhang N, Liao S-Y, Tse H-F, Myocardial repair of bioengineered cardiac patches with decellularized placental scaffold and human-induced pluripotent stem cells in a rat model of myocardial infarction, Stem Cell Res. Ther. 12 (1) (2021) 13. [PubMed: 33413626]

[46]. Neelakantan S, Kumar M, Singh R, Koch SE, Rubinstein J, Burton AJ, Sadayappan S, Avazmohammadi R, Abstract p3022: multiscale characterization of left ventricular diastolic dysfunction in diabetic and cardiac myosin binding protein-c phospho-ablated murine models, Circ. Res. 131 (Suppl_1) (2022) AP3022.

[47]. Avazmohammadi R, Mendiola EA, Li DS, Vanderslice P, Dixon RAF, Sacks MS, Interactions between structural remodeling and hypertrophy in the right ventricle in response to pulmonary arterial hypertension, J. Biomech. Eng. 141 (9) (2019).

[48]. Babaei H, Mendiola EA, Neelakantan S, Xiang Q, Vang A, Dixon RAF, Shah DJ, Vanderslice P, Choudhary G, Avazmohammadi R, A machine learning model to estimate myocardial stiffness from EDPVR, Sci. Rep. 12 (1) (2022) 5433. [PubMed: 35361836]

[49]. Zhang Y, Adams J, Wang VY, Horwitz L, Tartibi M, Morgan AE, Kim J, Wallace AW, Weinsaft JW, Ge L, et al. , A finite element model of the cardiac ventricles with coupled circulation:

Biventricular mesh generation with hexahedral elements, airbags and a functional mockup interface to the circulation, Comput. Biol. Med. 137 (2021) 104840. [PubMed: 34508972]

[50]. Harrison SM, Bers DM, Influence of temperature on the calcium sensitivity of the myofilaments of skinned ventricular muscle from the rabbit, J. Gen. Physiol. 93 (3) (1989) 411–428. [PubMed: 2703821]

[51]. Sweitzer NK, Moss RL, The effect of altered temperature on Ca2(+)-sensitive force in permeabilized myocardium and skeletal muscle. Evidence for force de- pendence of thin filament activation, J. Gen. Physiol. 96 (6) (1990) 1221–1245. [PubMed: 2286833]

## Statement of significance

Heart failure cause significant alterations to the contractile-relaxation behavior of the myocardium. Multiscale characterization of the contractile behavior of the myocardium is essential to advance our understanding of how contractility translates from fiber to organ and to identify the multiscale mechanisms leading to impaired cardiac function. While passive myocardial behavior has been studied extensively, the investigation of tissue-level contractile behavior remains critically scarce in the literature. To the best of our knowledge, our study here is the first to investigate the contractile behavior of the left ventricle at multiple length scales in small animals. Our results indicate that the active myocardial wall is a function of transmural depth and relaxes faster in the direction with larger peak stresses.

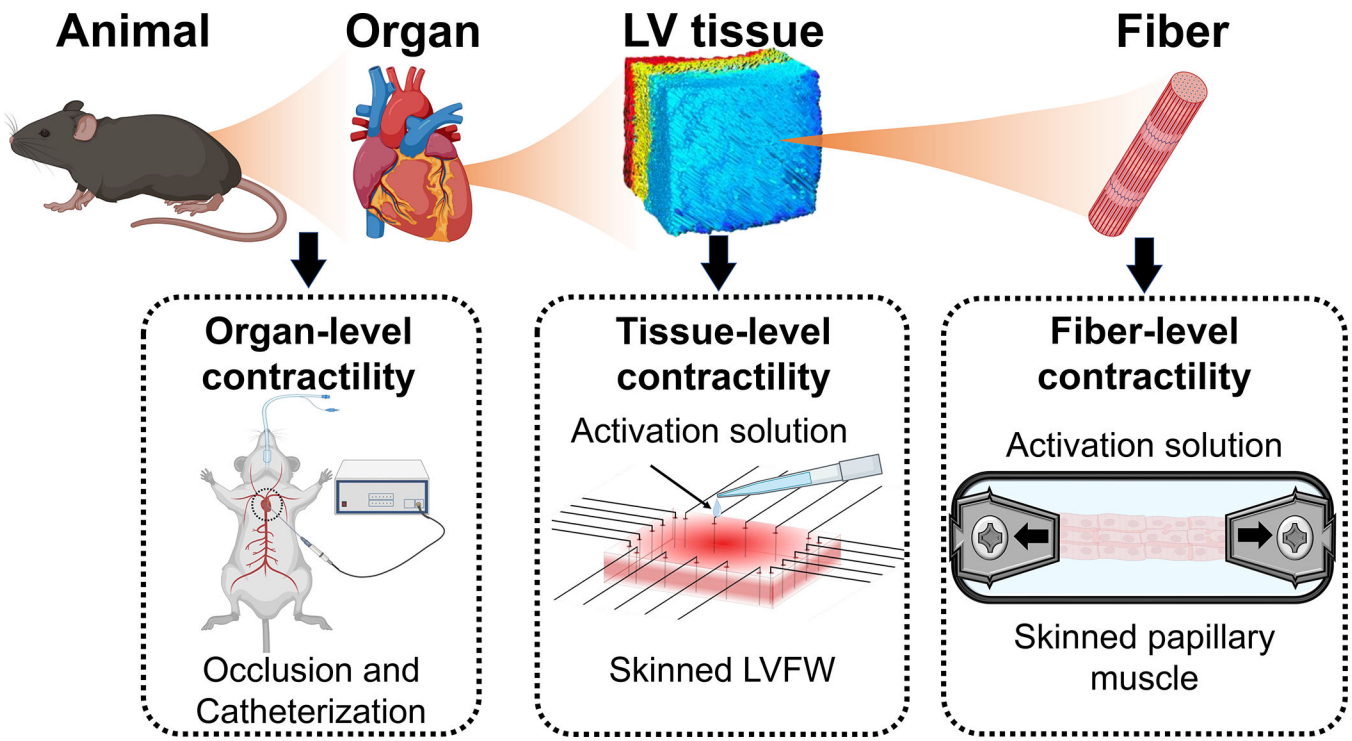


**Fig. 1.**
Overview of the multiscale characterization of contractile behavior of the myocardium.

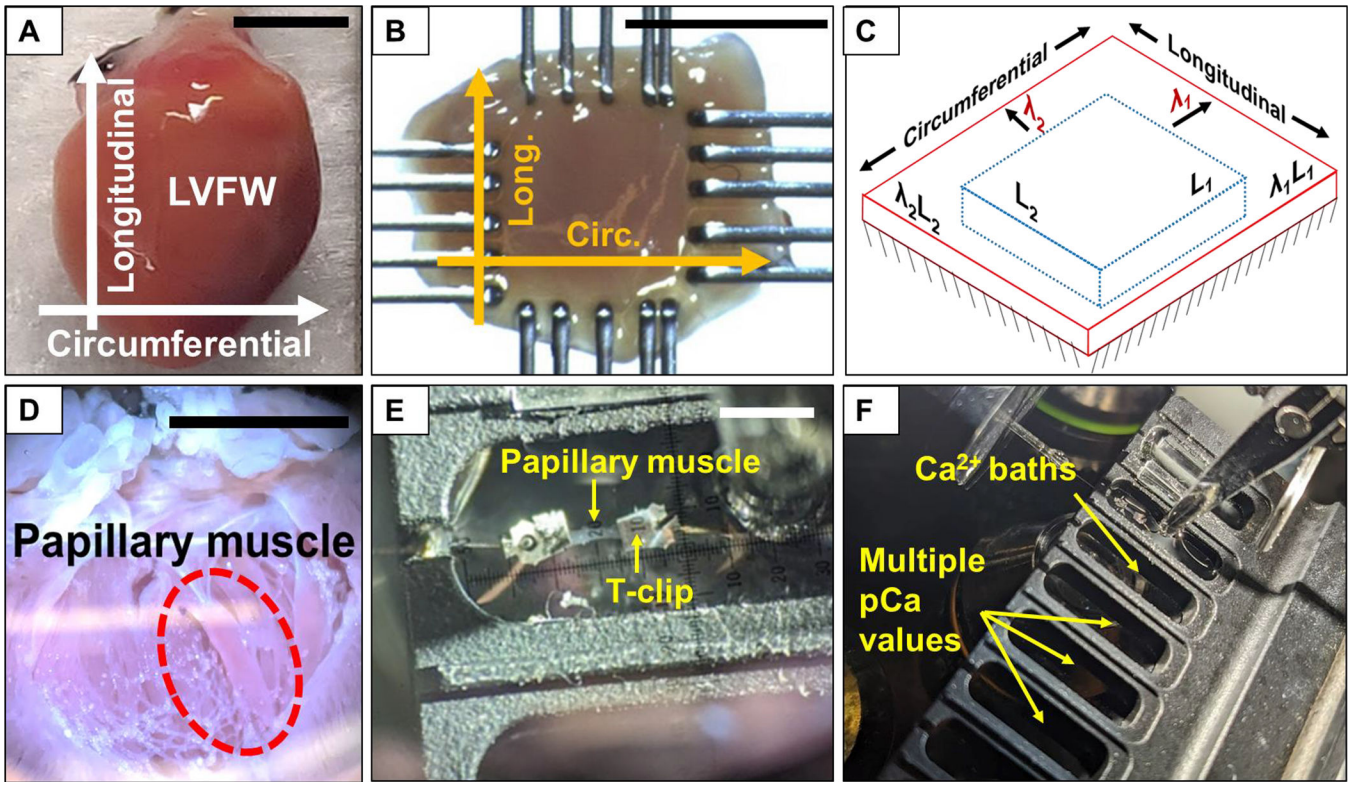


**Fig. 2.**

Overview of steps in the testing process. (**A**) Heart with designated orientations. (**B**) Mounted LVFW specimen post-skinning with orientations labeled. (**C**) Schematic of stretching and activation test protocol. Specimens were passively stretched to $\lambda_1$ and $\lambda_2$ in the circumferential and longitudinal directions, respectively, prior to active isometric contraction. (**D**) Image of an open heart for papillary muscle extraction. (**E**) Papillary muscle mounted to the testing device using aluminum T-clips prior to active isometric contraction. (**F**) Movement of mounted papillary muscle specimen through baths with different $Ca^{2+}$ concentration levels. Scale bars in A, B, D, E: 5 mm.

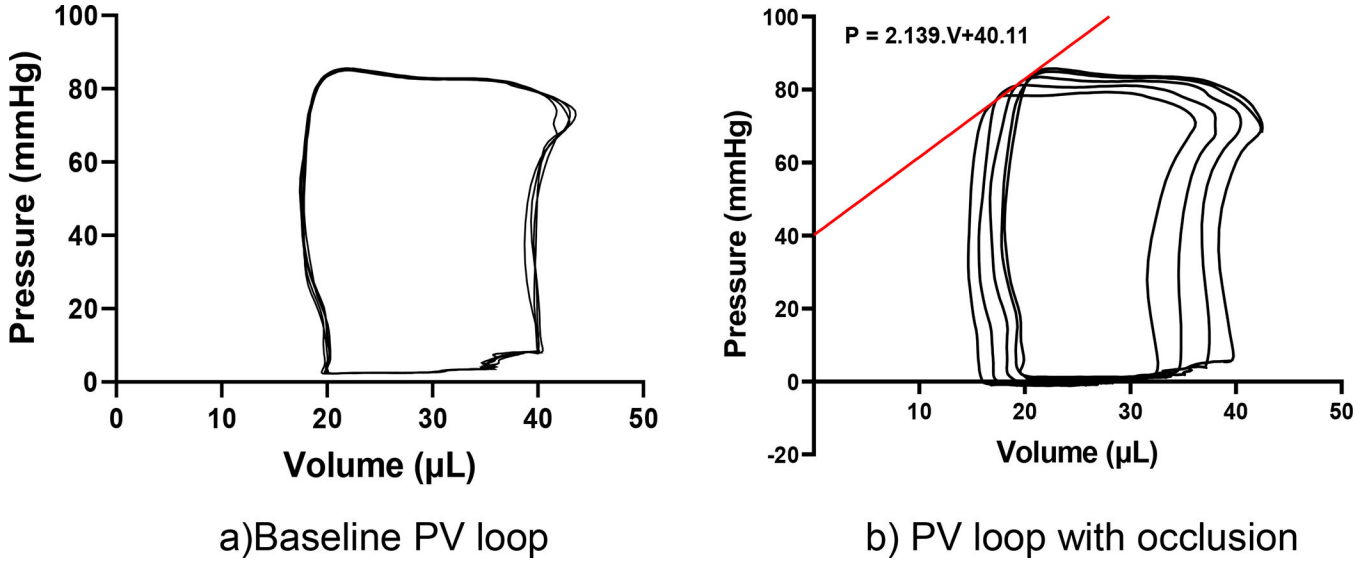


**Fig. 3.**

(**A**) Representative P-V loops from baseline left heart catheterization. (**B**) representative P-V loops during inferior vena cava occlusion, the red line indicates the end-systolic pressure-volume relationship (ESPVR). The organ-level contractility, measured by end-systolic elastance ($E_{es}$), from the slope of the representative ESPVR line was 2139 mmHg/ml.

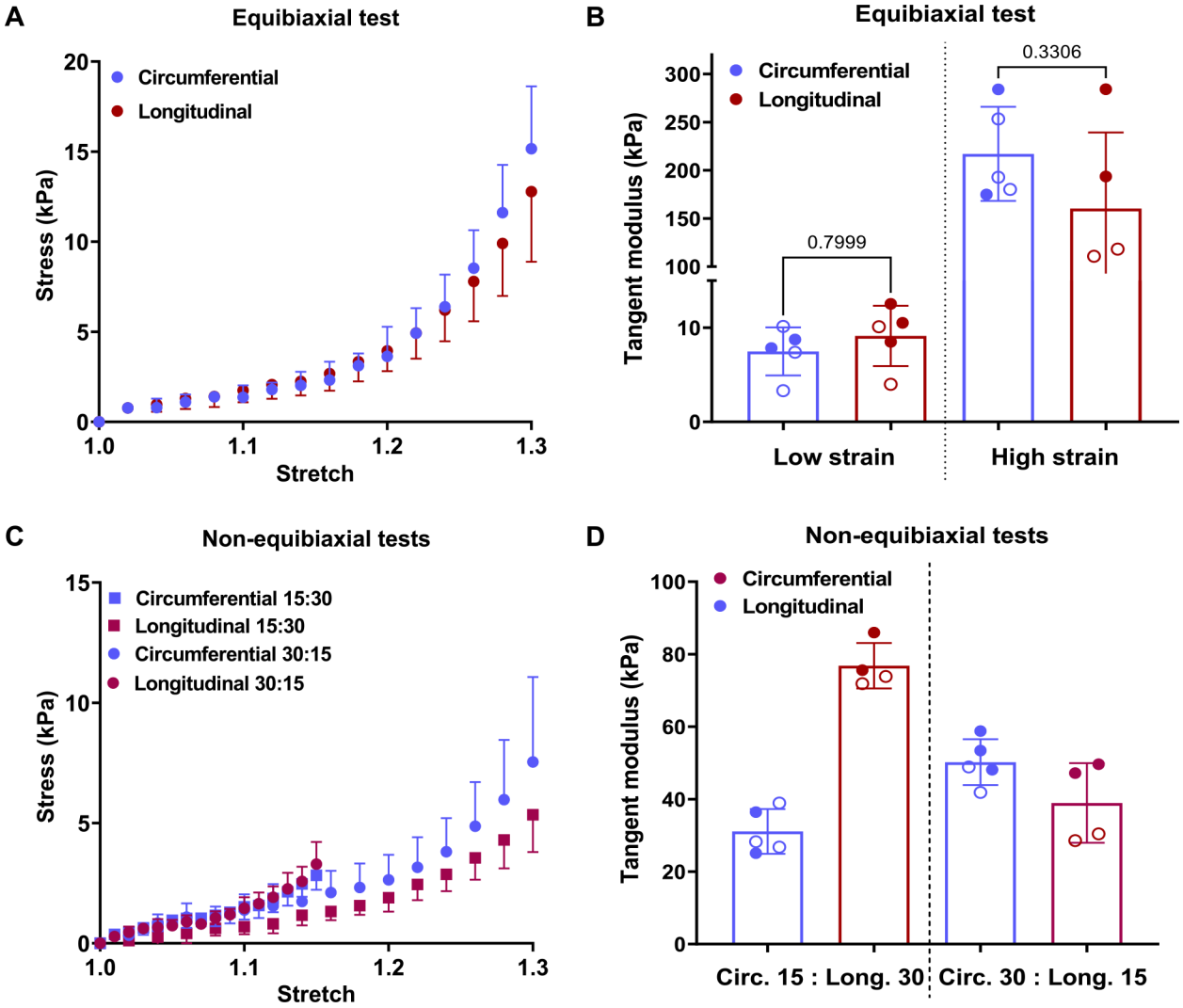


**Fig. 4.**

Equibiaxial (**A**) stress-stretch behavior and (**B**) tangent modulus of the LVFW. (**C**) Non-equibiaxial stress-stretch curves where the circles denote tests where circumferential: longitudinal stretch is 30%:15% while the squares denote the test where the stretch ratios are the reverse and (**D**) the tangent modulus of the LVFW. Paired t-test was performed to determine the statistical significance between the circumferential and longitudinal directions in Parts (B). Statistical comparisons are not reported in (D) because the circumferential and longitudinal stresses were obtained under different stretch values. Stress calculated is 1st-PK stress. The filled and hollow markers indicate male and female specimens, respectively.

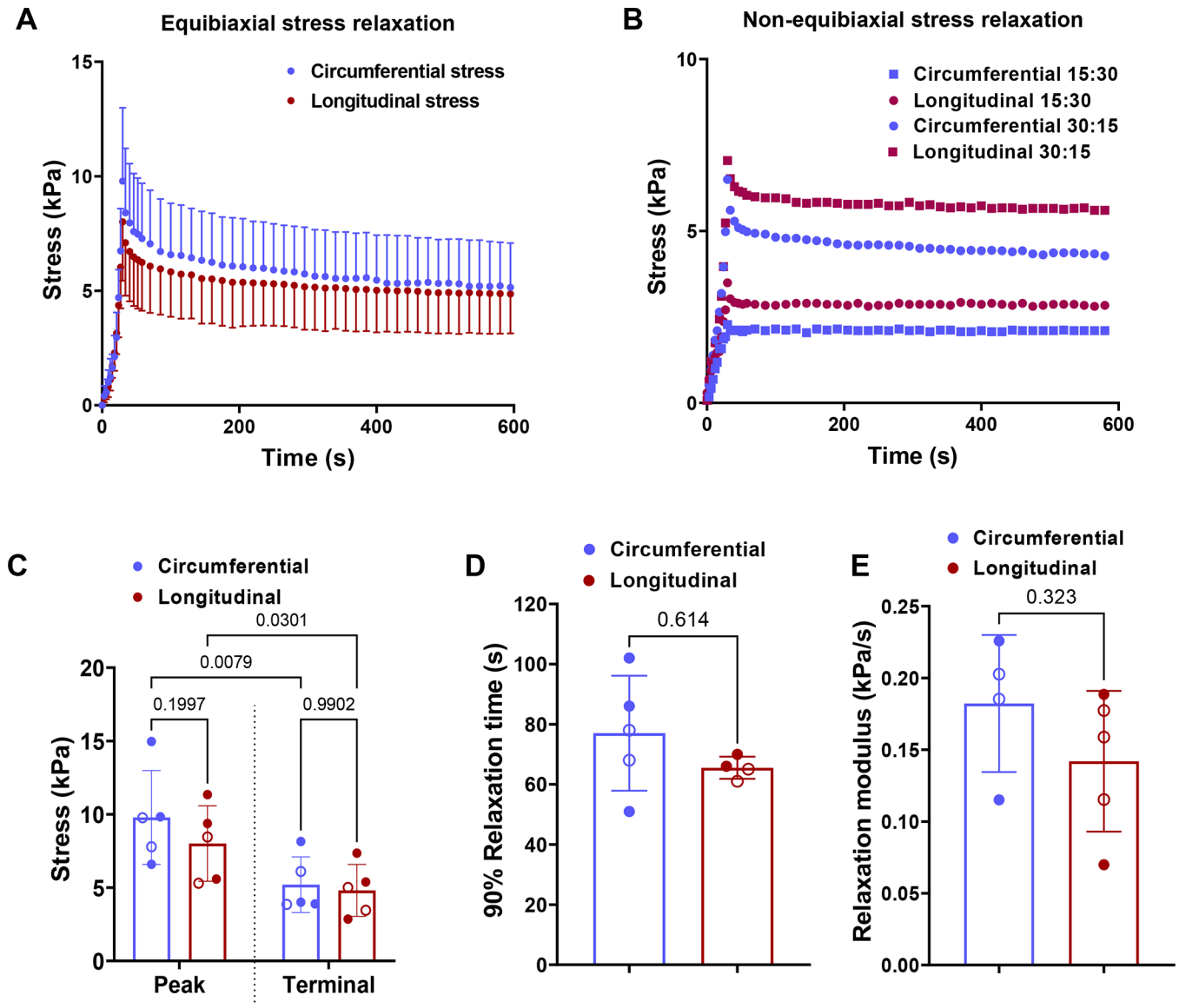


**Fig. 5.**

(**A**) Equibiaxial stress relaxation curves. (**B**) Non-equibiaxial stress relaxation curves where the circles denote tests where circumferential:longitudinal stretch is 30%:15% while the squares denote the test where the stretch ratios are the reverse. (**C**) Mean peak and terminal stress values. Terminal stress is measured at $t = 600$ s. (**D**) Relaxation time and (**E**) relaxation modulus calculated as the slope of the stress-time curve at the start of relaxation. Two-way ANOVA with repeated measures was used to perform statistical analysis in (C). Paired t-tests were performed to determine the statistical significance between the circumferential and longitudinal directions in (D) and (E). Stress calculated is 1st-PK stress. The filled and hollow markers indicate male and female specimens, respectively.

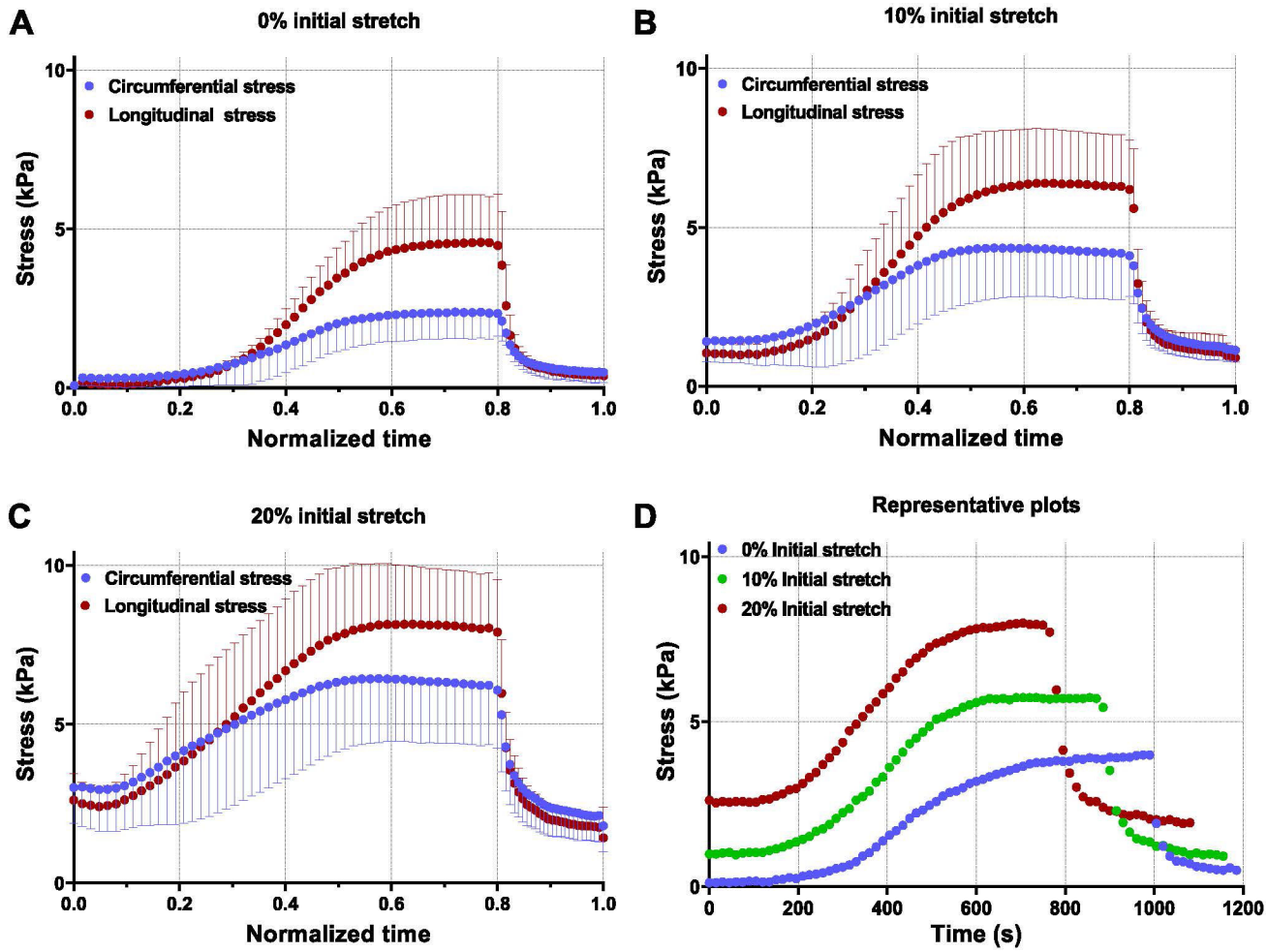


**Fig. 6.**

Active contractile behavior ($n = 6$) at pre-stretch values of (**A**) no pre-stretch, (**B**) 10% pre-stretch, (**C**) 20% pre-stretch. (**D**) Representative curves at multiple pre-stretch values indicate the change in the time required to reach peak stress. Specimens with initial stretched were allowed to undergo viscoelastic relaxation before being submerged in $Ca^{2+}$. Stress calculated is 1st-PK stress.

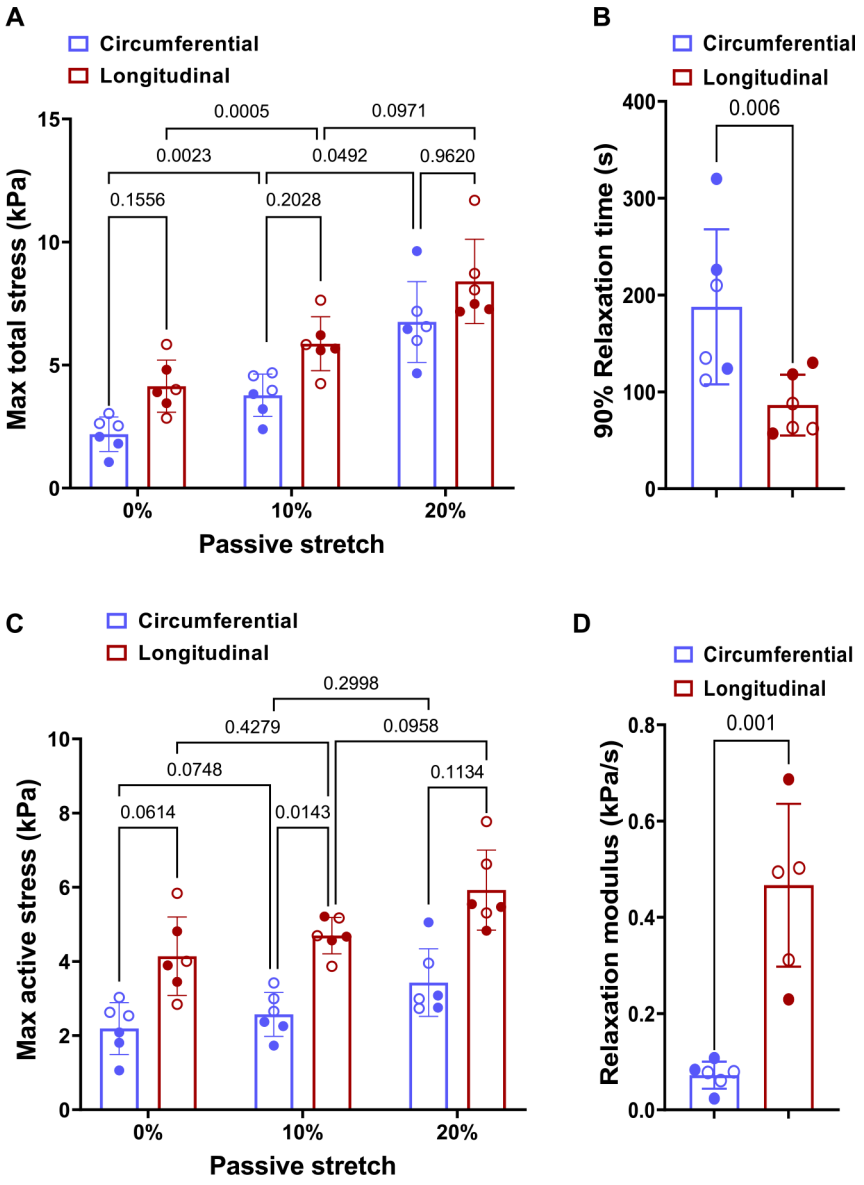


**Fig. 7.**

(**A**) Effect of passive stretch on the total stress during active contraction. (**B**) Time to relax 90% in the circumferential and longitudinal directions, (**C**) Effect of passive stretch on active stress and (**D**) The relaxation modulus in the circumferential and longitudinal directions with no initial stretch. The filled and hollow markers indicate male and female specimens, respectively. Stresses presented in this figure are the 1st-PK stress. Two-way ANOVA with repeated measures was used to perform statistical analysis in (A) and (C). Paired t-tests were performed to determine the statistical significance between the circumferential and longitudinal directions in (B) and (D).

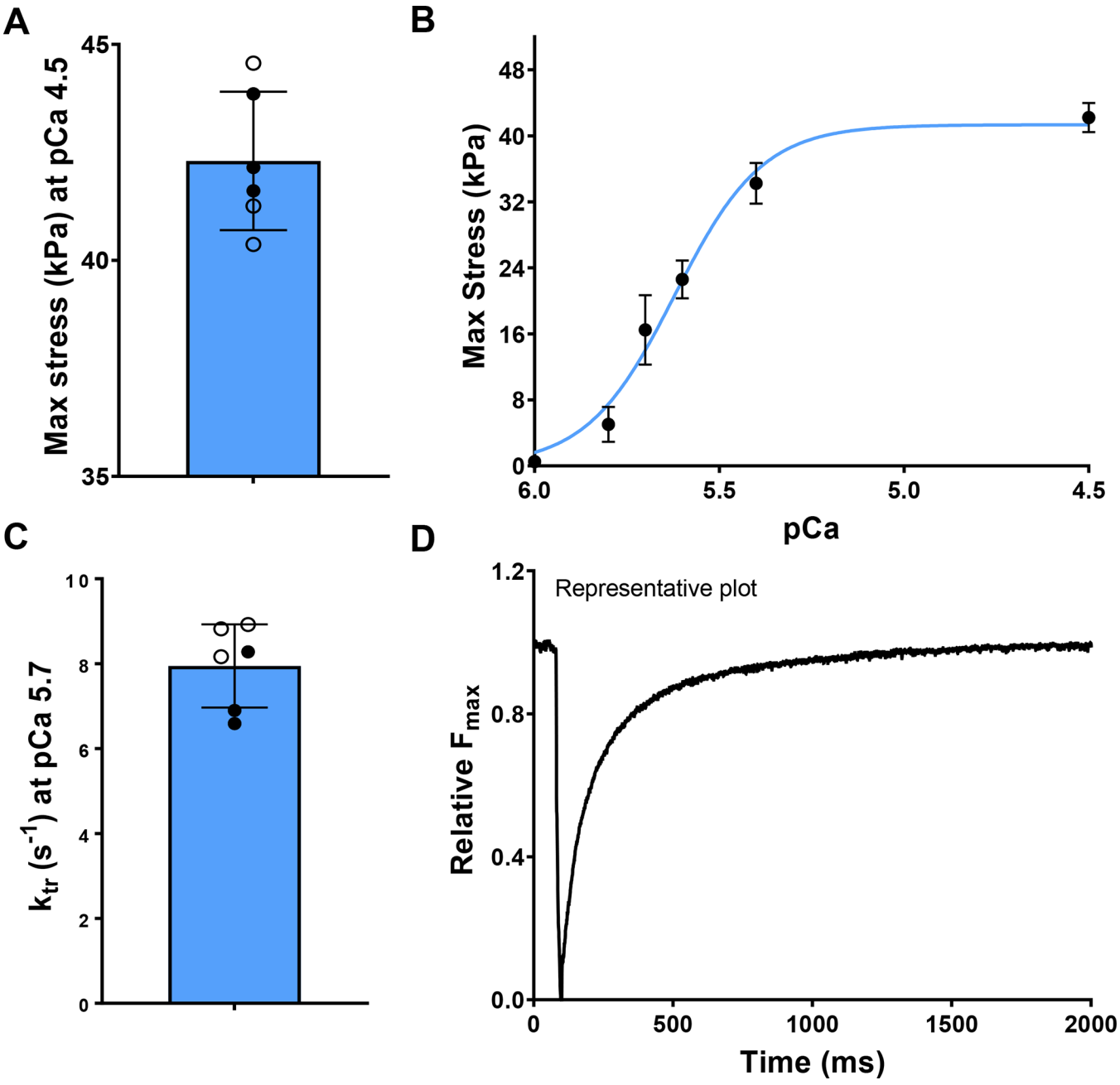


**Fig. 8.**

(**A**) The maximum contractile stress developed in the papillary muscle. (**B**) The effect of extrinsic $Ca^{2+}$ concentration on maximum contractile stress ($n = 6$). (**C**) The rate of force development after cross-bridge dissociation, and (**D**) representative time for force development after cross-bridge dissociation. The filled and hollow markers indicate male and female specimens, respectively.

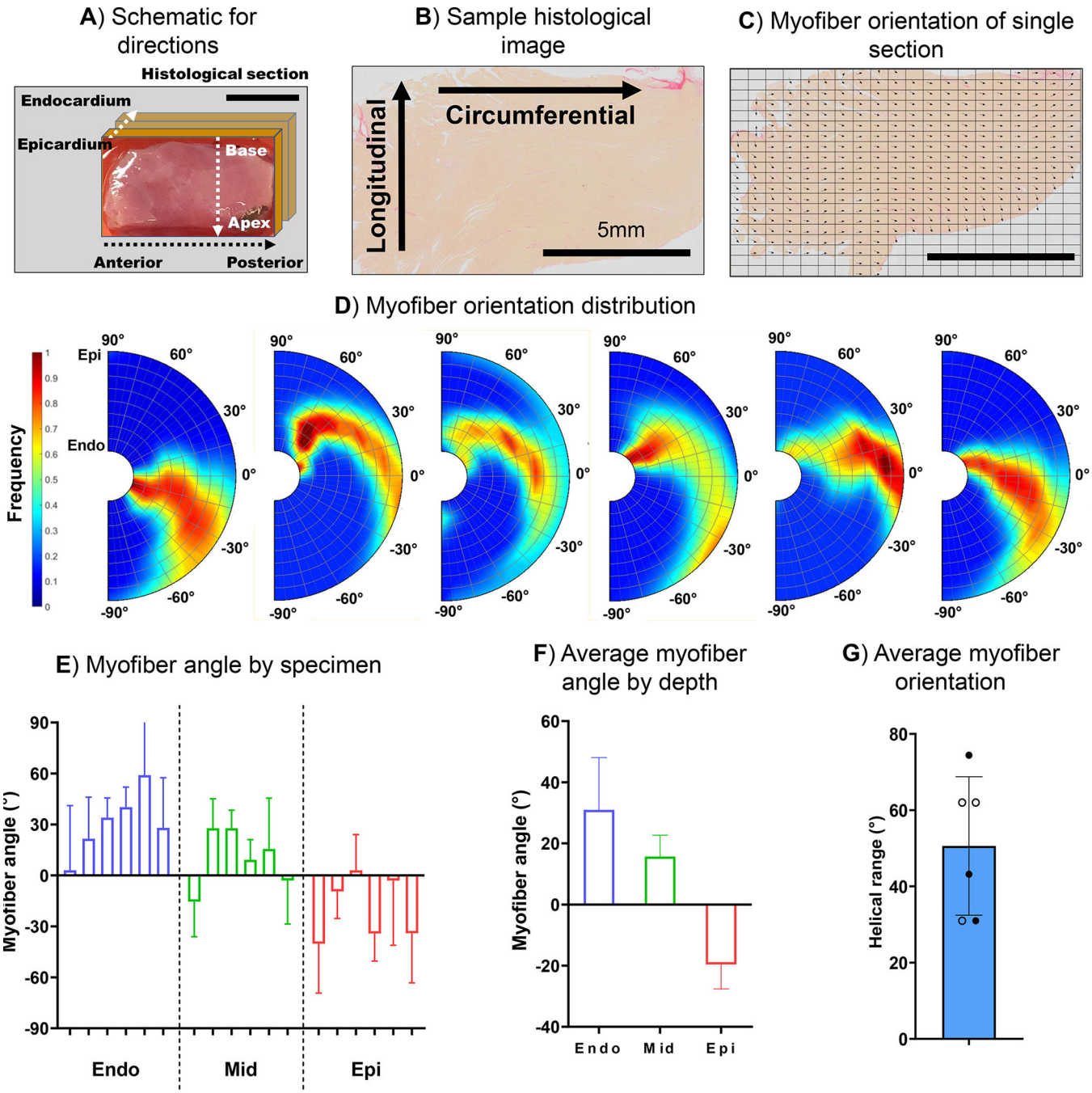


**Fig. 9.**

(**A**) Representative schematic of the circumferential (anterior to posterior), longitudinal (apex to base), and transmural directions (epicardium to endocardium). (**B**) Representative histological slide images of the cardiac tissue stained with picrosirius red (PSR) and (**C**) the calculated myofiber direction marked with vectors. (**D**) Transmural myofiber orientations. (**E**) The average myofiber angle by specimen and by depth (mean and standard deviation obtained from Beta distribution), (**F**) the average myofiber angle by depth-averaged over the six specimens, and (**G**) the helical range (the angle of rotation of the fibers from the

endocardium to the epicardium). The filled and hollow markers indicate male and female specimens, respectively. Scale bar in (A), (B), and (C): 5mm.

**Table 1**

Hemodynamic parameters obtained from catheterization and echocardiography. LV: left ventricle, EF: ejection fraction, ESP: end-systolic pressure, EDP: end-diastolic pressure.

| **Parameter** | **Value (*n* = 8)** |
|---|---|
| LVEF (%) | 75.42 ± 5.17 |
| LV ESP (mmHg) | 87.41 ± 5.45 |
| LV EDP (mmHg) | 8.66 ± 1.86 |
| $P_{max}$ (mmHg) | 89.39 ± 5.11 |
| $dP/dt_{max}$ (mmHg/s) | 5831.1 ± 517.33 |